Journal of the Optical Society of America A
OPTICS, IMAGE SCIENCE, AND VISION

Aero-optical effects, part I. System-level considerations: tutorial

MATTHEW KALENSKY,[1] STANISLAV GORDEYEV,[2] MATTHEW R. KEMNETZ,[3] AND MARK F. SPENCER[4,*]

[1]Integrated Engagement Systems Department, Naval Surface Warfare Center Dahlgren Division, Dahlgren, Virginia 22448, USA
[2]Department of Aerospace and Mechanical Engineering, University of Notre Dame, Notre Dame, Indiana 46556, USA
[3]Directed Energy Directorate, Air Force Research Laboratory, Albuquerque, New Mexico 87108, USA
[4]Joint Directed Energy Transition Office, Office of the Under Secretary of Defense for Research and Engineering, Washington, District of Columbia 20301-3030, USA
*mark.spencer@osamember.org

Received 25 June 2024; revised 14 September 2024; accepted 30 September 2024; posted 1 October 2024; published 22 October 2024

This paper serves as part I of a two-part tutorial on "aero-optical effects." We first present background information to assist with our introduction of the topic. Next, we use the aerodynamic environment associated with a hemisphere-on-cylinder beam director to decompose the resulting aberrations (that arise due to aero-optical effects) in terms of piston, tilt, and higher-order phase errors. We also discuss the performance implications that these phase errors have on airborne-laser systems. Recognizing the complexity of these environments, we then discuss how one measures these phase errors using standard wavefront-sensing approaches and the impact these phase errors have on imaging performance. These system-level considerations provide the material needed to survey several sources of aberrations such as boundary layers and shear layers, as well as mechanical contamination, shock waves, and aero-acoustics—all of which we cover in part II of this two-part tutorial.

https://doi.org/10.1364/JOSAA.533763

1. INTRODUCTION

There has been significant interest in airborne-laser systems in the United States since the Airborne Laser Laboratory (ALL) in the late 1970s and early 1980s [1,2]. Accordingly, researchers began to study the deleterious effects caused by the aerodynamic environment [3–10]. The ALL program used a CO_2 laser, which lased at a central wavelength of 10.6 μm. Overall, the ALL program was highly successful; however, researchers believed that in order to increase the capability of future airborne-laser systems, they would need to use shorter-wavelength lasers [7,9,11,12].

In the absence of aberrations, shorter-wavelength lasers result in higher peak irradiance (at the observation plane) given the same aperture diameter and laser power (in the pupil plane) [13,14]. As such, interest and research gravitated towards the use of short wave infrared (SWIR) lasers. Since the days of ALL, airborne-laser systems have steadily decreased in laser wavelength. For example, the airborne laser used a chemical oxygen-iodine laser, which lased at a central wavelength of 1.3 μm [15]. The latest development of high-power, solid-state lasers uses an even shorter central wavelength of 1.03–1.08 μm.

Unfortunately, shorter-wavelength lasers are more susceptible to the deleterious effects caused by the aerodynamic environment [7,11,12]. When researchers use shorter-wavelength lasers, the resulting aberrations caused by the air flow in proximity of the beam director become an even greater driver for performance at the system level. Thus, extensive research ensued in a field commonly referred to as "aero-optics" [11,16–25].

In the last 20 years, several comprehensive reviews have been written on the subject of aero-optical effects [12,21,26–29]. These reviews often present material on the state of the art within the aero-optics field. With that said, this paper differs from these reviews and serves as part I of a two-part tutorial on aero-optical effects. Consistent with other tutorials (e.g., Refs. [30,31]), the material presented in this paper provides the underlying tools needed to comprehend the more-advanced material contained within these reviews, as well as a recently published book [32], which also serves as an excellent source of information.

This two-part tutorial also differs from previous efforts in that it (1) includes very detailed explanations on both the aerodynamic and optical effects, specifically for new researchers trying to investigate this field; (2) discusses recent results related to aero-optical effects at supersonic and hypersonic speeds, in addition to subsonic speeds; and (3) introduces the aero-optical effects associated with shock waves, mechanical contamination, and aero-acoustics, which all lead to aberrations that degrade performance at the system level. As such, (1)–(3) will inform

future efforts looking to implement laser systems on airborne platforms.

In what follows, Section 2 introduces the basic concepts needed throughout this two-part tutorial. Section 3 then introduces the classic hemisphere-on-cylinder beam director as an example turret geometry. The associated aerodynamic environment serves as a source for aberrations that we decompose into piston, tilt, and higher-order phase errors. In Section 4, we then discuss standard wavefront-sensing approaches used to measure these phase errors. We also discuss the impacts that these phase errors have on imaging performance. Finally, Section 5 summarizes and concludes part I of this two-part tutorial.

2. BACKGROUND

In this section, we introduce the background material necessary to describe the aero-optical effects discussed in the remainder of part I, as well as in part II of this two-part tutorial.

A. Aerodynamic Turbulence

For the case of an aircraft-mounted laser system, the aircraft is flying through the atmosphere displacing the fluid in its path. At low subsonic Mach numbers, the fluid displaces in a manner where the density of the fluid remains nearly unchanged (incompressible). However, as the Mach number M increases ($M \gtrapprox 0.3$), compressibility effects become non-negligible, and density varies across the flow field. When we propagate a laser beam through this variable-density field, the fluid imposes aero-optical effects onto the outgoing laser beam.

Before moving on, it is worth discussing the differences between aero-optical effects and atmospheric-optical effects. While both are due to density variations, there are several important distinctions that affect the way researchers analyze and model the resulting aberrations. First, the aberrations due to aero-optical effects typically result from a thin turbulent region near the aircraft (and result in isoplanatic or linear, shift-invariant phase errors), while the aberrations due to atmospheric-optical effects typically result from turbulence distributed along the propagation path (and result in anisoplanatic or linear, shift-varying phase errors). Second, as we will show later, aero-optical effects are due to pressure variations and compressibility effects at high-aircraft speeds, whereas atmospheric-optical effects are due to the variation of total temperature in the atmosphere [33,34]. Third, the relevant flow scales are quite different. Consistent with energy cascade theory [33,34], atmospheric-optical effects typically result from turbulent structures within the atmosphere. These structures are on the order of millimeters to hundreds of meters in scale (i.e., within the inertial subrange created by inner and outer scales). Aero-optical effects, on the other hand, typically result from turbulent structures that are highly dependent on the aerodynamic environment (e.g., the size and shape of the aerodynamic body). Nonetheless, these structures generally scale with the Mach number of the aircraft.

In addition to the above differences, aero-optical effects are statistically anisotropic and inhomogeneous. As such, different propagation directions and translations often yield statistically different aberrations. This last point will become apparent in the next section, where we discuss the aero-optical effects associated with a hemisphere-on-cylinder beam director. This outcome is not always the case with atmospheric-optical effects where we often assume statistically isotropic and homogeneous conditions. As a result, researchers can derive parameters like the Fried coherence diameter [35–37].

Several efforts have experimentally investigated the combined effects of propagating through both aero-optical and atmospheric-optical turbulence environments [38–40]. Regardless of the source, these density variations lead to corresponding fluctuations in the index of refraction. Throughout the rest of this tutorial, we specifically study how density variations lead to fluctuations in the index of refraction and the resulting aero-optical effects.

B. Gladstone–Dale Relation

If we project an initially unperturbed laser beam through a variable-density environment, then we subject the beam to index-of-refraction fluctuations in the fluid. We can relate the index-of-refraction fluctuations to the density variations using the Gladstone–Dale relation, given by

$$n(x, y, z, t) = 1 + K_{\mathrm{GD}}(\lambda)\rho(x, y, z, t), \tag{1}$$

where $n(x, y, z, t)$ is the space- and time-dependent index of refraction, $\rho(x, y, z, t)$ is the corresponding density field, and $K_{\mathrm{GD}}(\lambda)$ is the Gladstone–Dale constant, which is a function of wavelength λ [41,42]. In the visible to near infrared range, $K_{\mathrm{GD}}(\lambda)$ for dry air is approximately 2.27×10^{-4} m^3/kg [43]. In this tutorial, we assume the use of a quasi-monochromatic laser, allowing us to drop the dependence of K_{GD} on λ. In Eq. (1) and moving forward, the x- and y-directions describe a transverse plane, and the z-direction is along the direction of propagation.

C. Quantifying Aero-Optical Effects

For aerodynamic environments, the turbulent region is often relatively thin compared to the length of the propagation path. As such, we can use the paraxial approximation, since the irradiance of the complex-optical field stays relatively constant upon propagation through the turbulent region (see Refs. [27,32] for discussion regarding the validity of the paraxial approximation in quantifying aero-optical effects). Because of the aforementioned index-of-refraction fluctuations, the phase does not stay constant. We can quantify the severity of the phase errors (i.e., path-integrated deviations from constant phase) using the optical-path length (OPL) and the optical-path difference (OPD). In practice,

$$\mathrm{OPL}(x, y, t) = \int_0^Z n(x, y, z, t)\mathrm{d}z, \tag{2}$$

and OPD results from removing the spatial mean or piston from OPL, viz.

$$\begin{aligned}\mathrm{OPD}(x, y, t) &= \mathrm{OPL}(x, y, t) - \langle \mathrm{OPL}(x, y, t)\rangle_{x,y} \\ &= K_{\mathrm{GD}} \int_0^Z \rho'(x, y, z, t)\mathrm{d}z,\end{aligned} \tag{3}$$

where $\langle\cdot\rangle_{x,y}$ denotes a spatial average in the x- and y-dimensions and ρ' is the zero-mean fluctuating density field.

For collimated beams in the pupil plane of a laser system, we can relate $\mathrm{OPD}(x, y, t)$ to the wavefront error function $W(x, y, t)$ (denoted here in units of length) and the pupil-phase function $\phi(x, y, t)$ (denoted here in units of radians) using the following relationships:

$$\mathrm{OPD}(x, y, t) = -W(x, y, t) = -\phi(x, y, t)/k, \quad \textbf{(4)}$$

where $k = 2\pi/\lambda$ is the wavenumber. With Eq. (4) in mind, we primarily quantify aero-optical effects in terms of $\mathrm{OPD}(x, y, t)$ in this tutorial. This choice allows us to scale between different aerodynamic environments (as we will show in part II of this two-part tutorial).

The root mean square (RMS) of $\mathrm{OPD}(x, y, t)$ in the spatial dimensions yields $\mathrm{OPD}_{\mathrm{RMS}}(t) = \sqrt{\langle \mathrm{OPD}(x, y, t)^2 \rangle_{x,y}}$ and is an indication of the time-dependent departure from planarity. Furthermore, time averaging yields $\mathrm{OPD}_{\mathrm{RMS}} = \langle \mathrm{OPD}_{\mathrm{RMS}}(t) \rangle_t$, which is a quantity the aero-optics literature often refers to as "wavefront error" because of the relationships found in Eq. (4). In practice, $\mathrm{OPD}_{\mathrm{RMS}}$ is the most common metric for quantifying aero-optical effects. It is worth noting that we can relate the phase variance, σ_ϕ^2, to $\mathrm{OPD}_{\mathrm{RMS}}$ using the following relationship:

$$\sigma_\phi^2 = (k\mathrm{OPD}_{\mathrm{RMS}})^2. \quad \textbf{(5)}$$

This relationship is an important one to remember when describing performance at the system level.

D. System Performance

In this tutorial, we quantify system performance using the Strehl ratio (SR) [12], defined as

$$\mathrm{SR}(t) = \frac{I(t)}{I_Z}, \quad \textbf{(6)}$$

where $I(t)$ is the on-axis irradiance and I_Z is the diffraction-limited, on-axis irradiance (in the observation plane). If we focus a phase-error-free laser beam with a top-hat irradiance profile to the observation plane, the resultant irradiance pattern will be an "Airy Disc." In turn [14],

$$I_Z = \frac{P\pi D^2}{4\lambda^2 Z^2}, \quad \textbf{(7)}$$

where P is the laser power, D is the aperture diameter, and Z is the propagation distance. From Eq. (7), we can achieve an increased on-axis irradiance with more power, a larger aperture, a shorter wavelength, or a shorter propagation distance. With that said, system constraints with respect to size, weight, and power limit the size of the aperture diameter and the power of the laser. Therefore, the greatest opportunity for system improvement lies in using a shorter-wavelength laser. However, as discussed above, shorter-wavelength lasers are more susceptible to aero-optical effects.

We can use the extended Maréchal approximation [14,44] to directly relate σ_ϕ^2 to the time-averaged SR, viz.

$$\mathrm{SR} = \exp(-\sigma_\phi^2). \quad \textbf{(8)}$$

Recall that we can also relate σ_ϕ^2 to $\mathrm{OPD}_{\mathrm{RMS}}$ using the relationship found in Eq. (5). For the case of small effects (i.e., $\mathrm{OPD}_{\mathrm{RMS}} < 0.1\,\lambda\mathrm{m}$), Eq. (8) provides an excellent approximation. However, it is worth noting that the extended Maréchal approximation tends to underestimate the SR for large phase errors; however, the discrepancy is not large [44,45]. Using Eqs. (5), (7), and (8), we can illustrate the effect of varying laser wavelengths for diffraction-limited focused propagation and varying $\mathrm{OPD}_{\mathrm{RMS}}$ conditions. We present the results of this trade space in Fig. 1.

In the left plot of Fig. 1, we plot peak irradiance as a function of λ compared to a 1 μm case for diffraction-limited focused propagation. We see that in the absence of aero-optical effects, the on-axis irradiance markedly decreases with increasing λ (left to right). In the right plot of Fig. 1, we plot SR as a function of λ for different $\mathrm{OPD}_{\mathrm{RMS}}$ conditions ranging from 0.01 to 1 μm. While peak irradiance significantly decreases with increasing wavelength, when aberrations are present, shorter-wavelength lasers are more susceptible to degradations in system performance. For these reasons, it is important to understand the environments in which a laser system will operate. This last point will be the topic of discussion in the sections that follow.

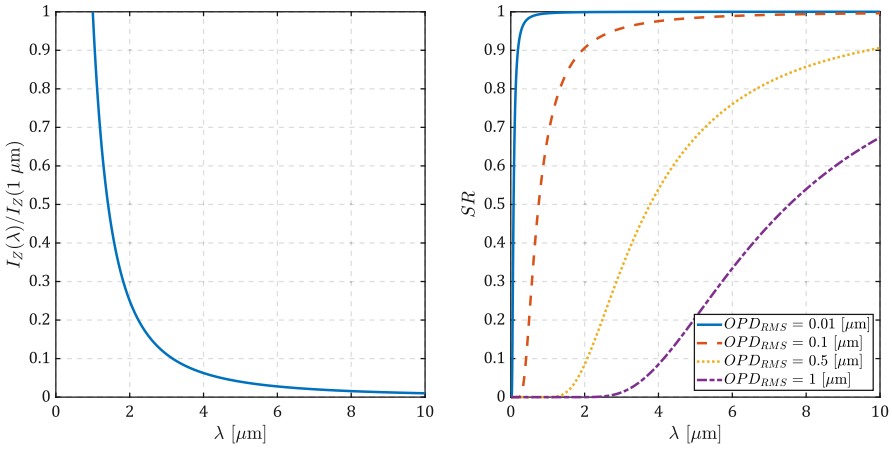

Fig. 1. Peak irradiance as a function of laser wavelength compared to a 1 μm laser for diffraction-limited focused propagation (left plot), and SR as a function of laser wavelength for varying $\mathrm{OPD}_{\mathrm{RMS}}$ conditions (right plot).

3. PHASE ERRORS

In this section, we use the aerodynamic environment associated with a hemisphere-on-cylinder beam director to decompose the resulting aberrations (that arise due to aero-optical effects) in terms of piston, tilt, and higher-order phase errors. After which, we discuss the performance implications that these phase errors have on airborne-laser systems.

A. Sources of Aberrations

The hemisphere-on-cylinder beam director has a simple turret geometry with a wide field of regard. In turn, this turret has been studied extensively for the past 20 years [26,46–58]. Upon mounting to a high-speed aircraft, the protrusion of the turret into the freestream flow creates a complicated aerodynamic environment, as shown in Fig. 2.

In Fig. 2, we depict the fluid-flow direction as going from top-left to bottom-right across the protruding beam director. An incoming freestream flow convects towards the turret, and an incoming boundary layer forms over the walls of the aircraft. We discuss the aero-optical effects associated with boundary layers in Sections 3.A and 3.B in part II of this two-part tutorial.

The incoming boundary layer stagnates on the lower frontal portion of the protruding beam director, which gives rise to a coherent vortical structure that extends around the sides of the turret. In contrast to the statistical-optics community, the fluid-mechanics community often uses the term "coherent" to describe turbulent structures. In a seminal paper, Hussain [59] defined a coherent structure as "a connected turbulent fluid mass with instantaneously phase-correlated vorticity over its spatial extent." For the purposes of this tutorial, we abide by this definition of coherent. With this definition in mind, we refer to the coherent vortical structure that extends around the sides of the turret geometry as a "necklace" vortex.

The fluid incident on the upper frontal part of the protruding beam director stagnates and then accelerates over the top of the hemispherical body. This frontal region of the turret is fairly steady, with only a thin boundary layer developing over it. The fluid that convects over the top of the turret geometry eventually separates due to an increase in static pressure as a function of streamwise location. Fluid separation leads to vortex shedding off the turret body. The Reynolds number, which describes the ratio of inertial to viscous forces in a fluid, dictates the onset of fluid separation.

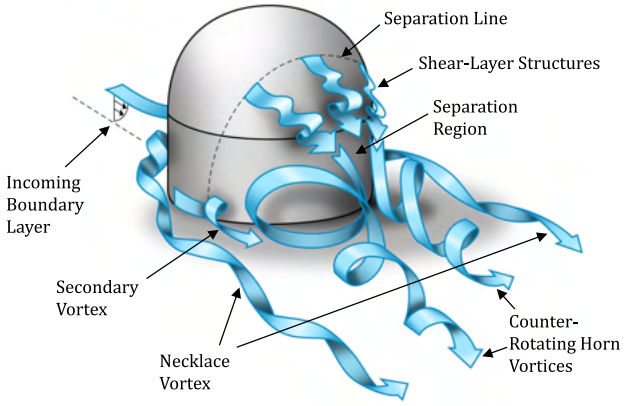

Fig. 2. Aerodynamic environment associated with a hemisphere-on-cylinder beam director. The inspiration for this illustrative example comes from Fig. 2 in Ref. [26].

Researchers have shown that the flow dynamics around hemispherical turrets are similar to the flow dynamics around spheres, with the exception of the near-wall region. The shedding around spheres starts at a Reynolds numbers based on the turret diameter, $Re_D \sim 400$ [60]. Therefore, one can expect a similar Re_D at which the shedding over turrets begins. If the incoming boundary layer is laminar before separation, the flow separates at ∼80 deg relative to the incoming freestream flow. At a sufficiently large Re_D ($\gtrsim 2 \times 10^5$), the boundary layer over the sphere becomes turbulent prior to separation. If the incoming boundary layer is turbulent before separation, the flow separates at approximately ∼120 deg relative to the incoming freestream flow [26]; however, this angle depends on other factors. In Fig. 2, we depict the separation line using a black dashed line.

Once the flow separates, a shear layer region forms between the high-speed freestream flow over the top of the protruding beam director and the low-speed flow in the separation region directly downstream of the turret. We extensively discuss the aero-optical effects associated with shear layers in Sections 3.C and 3.D in part II of this two-part tutorial.

Counter-rotating vortices referred to as "horn" vortices form in this wake region. At low Mach numbers, the turbulent structures in this wake are fairly symmetrical about the turret-geometry centerline. As the Mach number increases, the horn vortices lose their symmetry, and the vortices begin shedding off the sides of the turret in an alternating manner. The alternating shedding of the horn vortices gives rise to unsteady forcing [57,58]. This fluid-induced unsteady forcing on the turret leads to mechanical contamination in the airborne-laser system. We discuss the aero-optical effects associated with mechanical contamination in Section 4.A in part II of this two-part tutorial.

To further complicate matters, the protrusion of the turret into the freestream flow leads to a local acceleration of the fluid over its hemispherical body. When the incoming Mach number is greater than approximately 0.55, the accelerated flow becomes supersonic near the crown of the turret geometry, and a shock wave forms. Shock waves result in an extremely sharp change in gas properties across them; namely, a decrease in Mach number, increase in density, increase in pressure, and increase in temperature. The gas properties change across a region on the order of a few mean free paths of the gas, and as such, one can model them as a phase discontinuity [61]. We discuss the aero-optical effects associated with shock waves in Section 4.B in part II of this two-part tutorial.

Lastly, depending on the placement of the protruding beam director relative to the aircraft propulsion system, acoustic waves may also emanate past the turret [62]. In this case, aero-acoustic-induced pressure fluctuations can further degrade the performance of the airborne-laser system. We discuss the aero-optical effects associated with aero-acoustics in Section 4.C in part II of this two-part tutorial.

From Fig. 2, it is clear that the aerodynamic environment associated with a hemisphere-on-cylinder beam director gives rise to multiple sources of aberrations. In what follows, we broadly characterize these aberrations in terms of piston, tilt, and higher-order phase errors. For the reader looking for an

introduction to aberration theory, please see Ref. [63], for example.

B. Piston and Tilt Phase Errors

In Fig. 2, we can see that a backward-looking angle results in the outgoing laser beam propagating through significant aerodynamic turbulence. In what follows, we show that the beam diameter acts as a form of spatial filter where turbulence structures larger than the beam diameter manifest primarily as piston and tilt phase errors. We also discuss the performance implications of these phase errors on airborne-laser systems.

1. Description of Piston and Tilt Phase Errors

Piston and tilt phase errors represent the path-integrated effects of first-order aberrations. In order to describe these phase errors, we introduce the Zernike polynomial series. For a circular aperture of the diameter D we can describe the even and odd modes of the Zernike series by [64,65]

$$Z_n^m(r,\theta) = R_n^m(r)\cos(m\theta) \tag{9}$$

and

$$Z_n^{-m}(r,\theta) = R_n^m(r)\sin(m\theta), \tag{10}$$

respectively. Here, $R_n^m(r)$ is the radial polynomial function, given as

$$R_n^m(r) = \sum_{i=0}^{\frac{n-m}{2}} \frac{(-1)^i (n-i)!}{i!\left(\frac{n+m}{2}-i\right)!\left(\frac{n-m}{2}-i\right)!} r^{n-2i}. \tag{11}$$

We can describe piston, x-tilt, and y-tilt by the Zernike modes Z_0^0, Z_1^{-1}, and Z_1^1, respectively. With simplification, we can write these modes as $Z_0^0(r,\theta) = 1$, $Z_1^1(r,\theta) = (4r/D)\cos(\theta)$, and $Z_1^{-1}(r,\theta) = (4r/D)\sin(\theta)$.

Using the approach taken by Sasiela [65], the spatial-wavenumber-dependent aperture filter function $F(\kappa)$ to remove piston and the x- and y-components of tilt takes the following form:

$$F(\kappa) = 1 - \left[\frac{2J_1(\kappa D/2)}{\kappa D/2}\right]^2 - \left[\frac{4J_2(\kappa D/2)}{\kappa D/2}\right]^2, \tag{12}$$

where $J_\nu(\cdot)$ is the Bessel function of the first kind, and the subscript ν denotes the order of the Bessel function. Making the change of variables $\Lambda = 2\pi/\kappa$, where Λ is the optical-turbulence structure size, we plot Eq. (12) in Fig. 3 as a solid blue line. We also plot the first bracketed term in Eq. (12), which represents the piston filter function as a dashed-dotted red line, as well as the second bracketed term in Eq. (12), which represents the tilt filter function as a dotted yellow line.

In Fig. 3, we see the relationship introduced above; namely, the beam size acts as a form of high-pass spatial filter where turbulence-induced aberrations larger than the beam size ($\Lambda > D$) result in tilt and piston phase errors, and turbulence-induced aberrations smaller than the beam size become higher-order phase errors ($\Lambda < D$) [65,66]. In the limiting case of an infinitely large aperture, the aerodynamic turbulence imposes only higher-order phase errors onto the outgoing laser beam. Similarly, in the limiting case of an infinitely small aperture, the aerodynamic turbulence imposes only piston phase errors onto the outgoing laser beam.

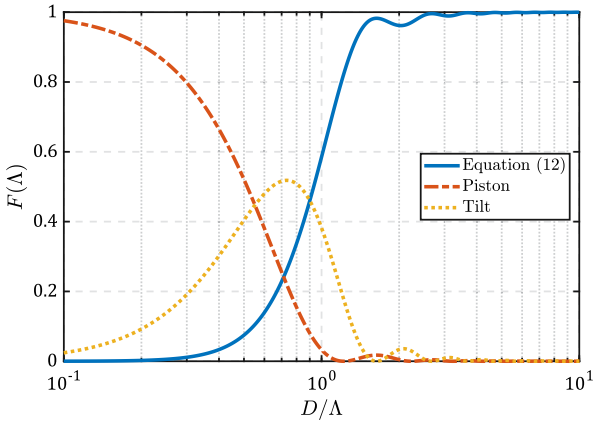

Fig. 3. Aperture filter function (to remove piston and tilt) as a function of D/Λ.

It is worth noting that for most applications involving laser beam propagation, a piston phase error does not affect system performance as it simply represents a net retardation of light due to propagation through non-vacuum mediums. Furthermore, piston phase errors are also difficult to sense using traditional wavefront sensing approaches. On the other hand, as we will show next, compensating for tilt phase errors is critically important for applications involving laser beam propagation.

2. Performance Implications of Tilt Phase Errors

To demonstrate the performance implications of tilt phase errors, we created a pupil-phase function (with a tilt phase error) in the top-left plot of Fig. 4. Here, the colorbar denotes wrapped phase in units of radians.

If we focus an outgoing laser beam with a top-hat irradiance profile to the observation plane, then the irradiance pattern due to a tilt phase error will be a "shifted Airy Disc." We present the corresponding object-plane irradiance pattern in the top-right plot of Fig. 4. Also plotted is a white circle with an Airy disk radius of $1.22\lambda Z/D$. This circle represents the diffraction-limited bucket and gives us a gauge for system performance.

On a long-exposure basis, tilt phase errors result in an effectively larger observation-plane irradiance pattern. We show an example of this dynamic in the bottom-left plot of Fig. 4. Here, we can see that the long-exposure, observation-plane irradiance pattern encompasses an area much larger than the diffraction-limited bucket (white circle).

If we employ tilt compensation to minimize the effects of tilt phase errors, then we can stabilize the observation-plane irradiance pattern to an on-axis aim point. We present the object-plane irradiance pattern after tilt compensation in the bottom-right plot of Fig. 4. Here, we can see that uncompensated tilt still remains on the outgoing laser beam, but a larger portion of the long-exposure, observation-plane irradiance pattern falls within the diffraction-limited bucket (white circle).

All four quadrants of Fig. 4 imply that effective tilt compensation results in a smaller residual tilt variance and leads to

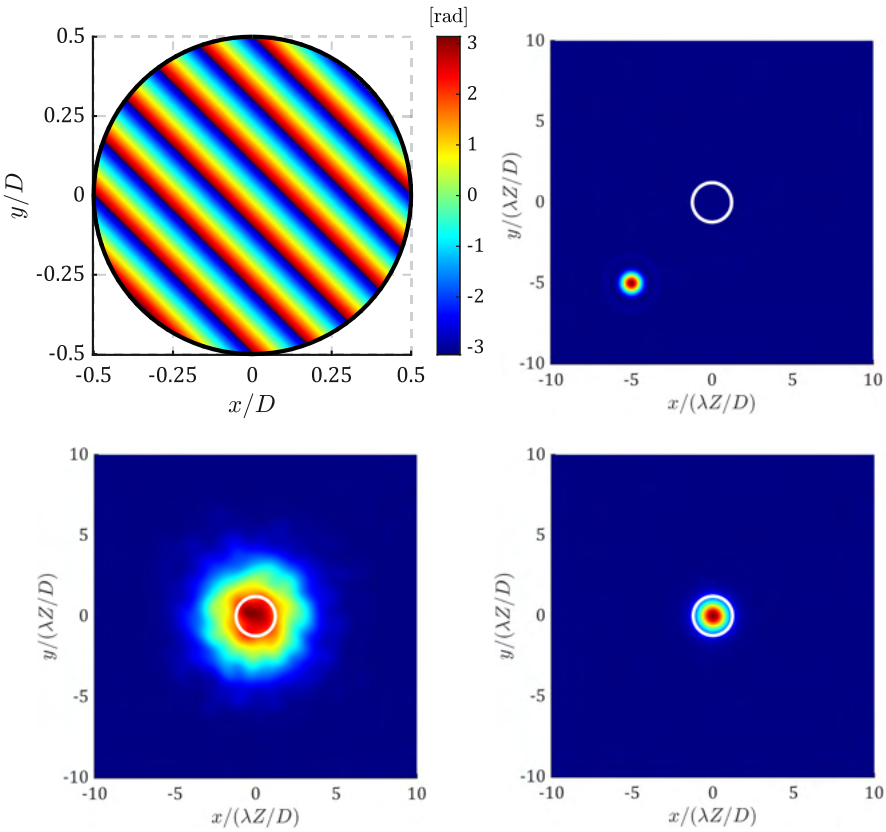

Fig. 4. Pupil-phase function with a tilt phase error (top left); corresponding object-plane irradiance pattern (top right); long-exposure, object-plane irradiance pattern (bottom left); and long-exposure, object-plane irradiance pattern after tilt compensation (bottom right).

increased system performance. It should be noted that system designers can effectively predict this outcome using Eq. (8). Thus, when designing future airborne-laser systems, it is of utmost importance that system designers account for the effects of tilt phase errors. Part II of this two-part tutorial will further expand on the sources of aberrations that give rise to tilt phase errors.

C. Higher-Order Phase Errors

Recall from Fig. 2 that at backward-looking angles, the laser beam propagates through significant aerodynamic turbulence. Also recall from Fig. 3 that turbulence structures smaller than the beam diameter impose higher-order phase errors onto the outgoing laser beam. In what follows, we describe these phase errors using proper orthogonal decomposition (POD) and discuss their performance implications on airborne-laser systems.

1. Description of Higher-Order Phase Errors

As discussed in Section 2.C, $\mathrm{OPD}_{\mathrm{RMS}}$ is the most common metric for quantifying aero-optical effects, and we can report $\mathrm{OPD}_{\mathrm{RMS}}$ with or without tilt. From Fig. 3, we saw that larger apertures will contain more higher-order phase errors, and subsequently, will have a larger tilt-removed $\mathrm{OPD}_{\mathrm{RMS}}$ compared to smaller apertures. We can relate the tilt-removed $\mathrm{OPD}_{\mathrm{RMS}}$ to the aperture filter function, $F(\kappa)$, defined in Eq. (12), as

$$\mathrm{OPD}_{\mathrm{RMS}}^2 = 2\int S_W(\kappa)F(\kappa)\mathrm{d}\kappa, \tag{13}$$

where $S_W(\kappa)$ is the spatial-wavenumber-dependent power spectral density (including contributions from piston, tilt, and higher-order phase errors).

While $\mathrm{OPD}_{\mathrm{RMS}}$ is a helpful metric, and we can quickly relate it to parameters such as SR [see Eq. (12) and Fig. 1], it does not reveal anything about the spatial structure of the turbulence-induced aberrations. To address this concern, researchers often decompose higher-order phase errors into orthogonal spatial modes. One approach is to use the Zernike modes given in Eqs. (9)–(11), excluding the piston and tilt terms. While this approach has been used by researchers for decades, the Zernike modes have drawbacks, particularly, in environments where the turbulence-induced aberrations do not exhibit isotropic behavior.

Recognizing the drawbacks of the Zernike modes, other modal-analysis techniques have become popular in recent years [67]. One of these modal-analysis approaches is POD. Sometimes referred to as principal component analysis or Karhunen–Loève expansion (within the statistical-optics community), POD is a modal-analysis technique that decomposes data into an optimal basis set of orthogonal-spatial modes organized from highest to lowest energy. This technique has quickly gained popularity within the fluid-mechanics community for a few reasons. First, since researchers can identify and organize POD modes in order of decreasing energy, it easily

becomes apparent what the dominant or most energetic spatial features of a particular data set are or are not. Additionally, since these modes are spatially orthogonal, researchers can easily reconstruct a much lower-order data set containing most of the energy, which makes it a popular reduced-order modeling technique.

We only introduce POD here; however, much greater detail on this modal-analysis technique can be found in Ref. [67]. Furthermore, many examples of using POD analysis to study aero-optical effects can be found in Ref. [32].

We can use POD to decompose the pupil-phase function, $\phi(\boldsymbol{x}, t)$, into orthogonal spatial modes, $\varphi_n(\boldsymbol{x})$, with associated temporal coefficients, $a_n(t)$, as

$$\phi(\boldsymbol{x}, t) = \sum_{n=0}^{N} a_n(t)\varphi_n(\boldsymbol{x}). \tag{14}$$

We find the modes by solving the eigenvalue problem given by

$$\int \mathrm{d}\boldsymbol{x}' R(\boldsymbol{x}, \boldsymbol{x}')\varphi_n(\boldsymbol{x}') = \lambda_n \varphi_n(\boldsymbol{x}), \tag{15}$$

where $R(\boldsymbol{x}, \boldsymbol{x}')$ is the two-point correlation matrix, defined as $R(\boldsymbol{x}, \boldsymbol{x}') = \langle \phi(\boldsymbol{x}, t)\phi(\boldsymbol{x}', t)\rangle$. We find the temporal coefficients associated with each mode by projecting the mode of interest onto $\phi(\boldsymbol{x}, t)$, viz.

$$a_n(t) = \int \mathrm{d}\boldsymbol{x}\phi(\boldsymbol{x}, t)\varphi_n(\boldsymbol{x}). \tag{16}$$

Its eigenvalue contains the energy within each mode, which we can compute from the temporal coefficients as $\lambda_n = \langle a_n(t)^2\rangle$. We present various examples of using POD in part II of this two-part tutorial.

2. Performance Implications of Higher-Order Phase Errors

To demonstrate the performance implications of higher-order phase errors, we created a pupil-phase function (with higher-order phase errors) in the top-left plot of Fig. 5. Like in Fig. 4, the colorbar denotes wrapped phase in units of radians.

If we focus an outgoing laser beam with a top-hat irradiance profile to the observation plane, then the irradiance pattern due to the higher-order phase errors will be "scintillated." We present the corresponding object-plane irradiance pattern in the top-right plot of Fig. 5. Also plotted is a white circle with an Airy disk radius of $1.22\lambda Z/D$. Like in Fig. 4, this circle represents the diffraction-limited bucket and gives us a gauge for system performance.

On a long-exposure basis, higher-order phase errors result in an effectively larger observation-plane irradiance pattern. We show an example of this dynamic in the bottom-left plot of Fig. 5. Here, we can see that the long-exposure, observation-plane irradiance pattern encompasses an area much larger than the diffraction-limited bucket (white circle).

If we employ higher-order compensation to minimize the effects of higher-order phase errors, then we can reduce beam spreading in the observation-plane irradiance pattern about the

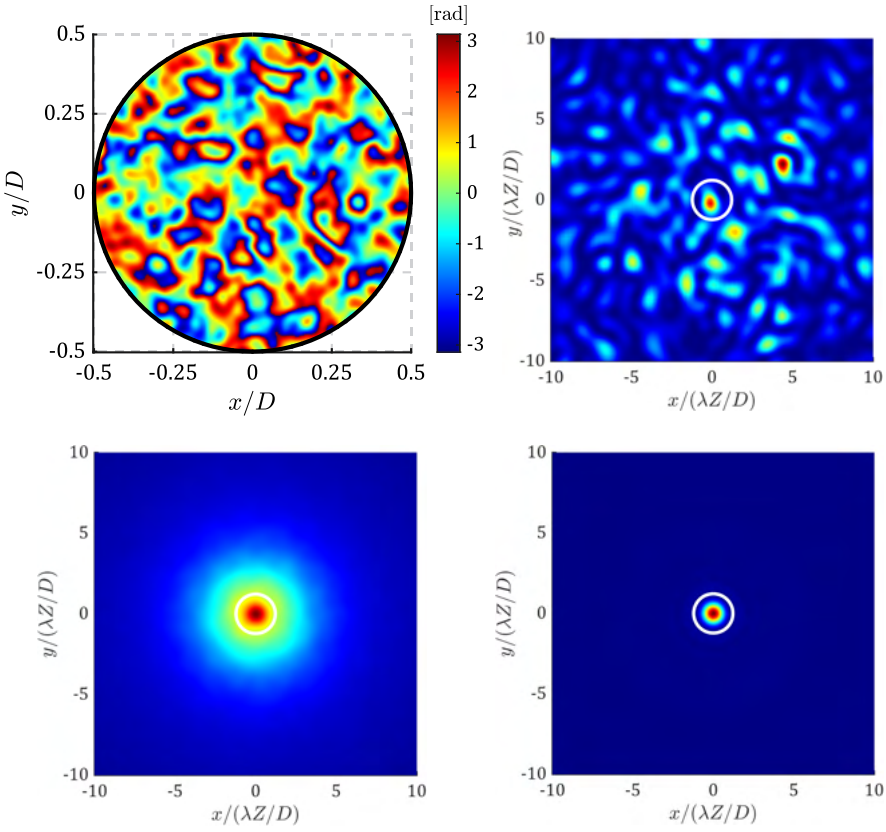

Fig. 5. Pupil-phase function with higher-order phase errors (top left); corresponding object-plane irradiance pattern (top right); long-exposure, object-plane irradiance pattern (bottom left); and long-exposure, object-plane irradiance pattern after higher-order compensation (bottom right).

aim point. We present the object-plane irradiance pattern after higher-order compensation in the bottom-right plot of Fig. 5. Here, we can see that with high-resolution phase compensation, the long-exposure, observation-plane irradiance pattern nearly falls within the diffraction-limited bucket (white circle).

All four quadrants of Fig. 5 imply that effective higher-order compensation results in a smaller residual phase variance (or tilt-removed $\mathrm{OPD}_{\mathrm{RMS}}$) and leads to increased system performance. It should be noted that system designers can effectively predict this outcome using Eq. (8). Thus, when designing future airborne-laser systems, it is of utmost importance that system designers account for the effects of higher-order phase errors. Part II of this two-part tutorial will further expand on the sources of aberrations that give rise to higher-order phase errors.

4. WAVEFRONT SENSING AND IMAGING

In this section, we introduce wavefront sensing approaches that have both pioneered and continue to advance the field of aero-optics. Furthermore, we discuss the performance impacts that aero-optical effects have on imaging performance.

A. Wavefront Sensing

Researchers can measure the phase errors induced by aerodynamic turbulence by using a wavefront sensor. As illustrated in Figs. 4 and 5, these phase errors are critical to measure in order to learn more about the aerodynamic environment. Wavefront sensing is a vast and active field of research in and of itself. As such, an in-depth review is beyond the scope of what we can cover in this tutorial. However, we can introduce two wavefront sensing approaches that have helped to build the knowledge we know today about the field of aero-optics. These two wavefront sensors are the Shack–Hartmann wavefront sensor (SHWFS) and the Malley probe. We also briefly introduce the digital-holographic wavefront sensor (DHWFS) as it has gained popularity in recent years and shows promise for supporting aero-optics experiments of the future.

1. Shack–Hartmann Wavefront Sensor

A SHWFS consists of an array of lenslets. In practice, researchers place these lenslets in a pupil plane of the airborne-laser system. They then place the sensor of a camera in an image plane that is conjugate to the focal length of these lenslets. In Fig. 4, we saw that pupil-plane tilt manifests as a shifted irradiance pattern (upon propagation to a focus). Accordingly, the lenslet array samples the phase errors such that primarily tilt phase errors remain across the subapertures. At focus, these pupil-plane tilts give rise to shifted irradiance patterns on the sensor of a camera.

Using the shifts or "deflections" of these irradiance patterns away from their on-axis locations, as well as the focal length of the lenslets, we can estimate the tilts or "deflection angles" $\theta_x(x, y, t)$ and $\theta_y(x, y, t)$. If the lenslets are uniformly illuminated, no discontinuities are present (like those experienced with shock waves), and the phase errors within the lenslets are not very energetic. Then,

$$\theta_x(x, y, t) = \frac{\partial \mathrm{OPD}(x, y, t)}{\partial x} \quad \text{and}$$

$$\theta_y(x, y, t) = \frac{\partial \mathrm{OPD}(x, y, t)}{\partial y}. \tag{17}$$

Subsequently, we can use $\theta_x(x, y, t)$ and $\theta_y(x, y, t)$ in a least-squares reconstruction algorithm to estimate $\mathrm{OPD}(x, y, t)$ [14,32].

Over the years, as sampling rates of digital cameras improved, the SHWFS became a viable instrument for characterizing aerodynamic environments. In conjunction with high-speed cameras, the SHWFS has enabled numerous wind-tunnel and flight-test experiments to be conducted. These experiments have helped to advance the knowledge of aero-optical effects. We discuss some of the analyses and findings that resulted from these experimental SHWFS measurements in part II of this two-part tutorial.

2. Malley Probe

As discussed above, the SHWFS uses high-speed cameras to collect time-resolved measurements. However, due to the inevitable compromise between spatial and temporal resolution, achieving a meaningful spatial resolution results in relatively slow sample rates (on the order of 20–50 kHz using commercial-off-the-shelf cameras). While these sampling rates are sufficient for studying subsonic aerodynamic environments, it might not be fast enough for sufficient temporal resolution at supersonic and hypersonic speeds. We can overcome this limitation by using a Malley probe instead of a SHWFS. Named after the work of Malley *et al.* [19] (who first proposed the technique), researchers, in practice, propagate a small-diameter laser beam through the environment of interest at a fixed spatial location x_0. They then focus this laser beam onto a measuring device using a lens.

By assuming that the phase errors of interest convect at a fixed speed U_C, we can use the time series of the measured deflection angles to estimate the one-dimensional OPD slice as

$$\theta_x(x_0, t) = \left.\frac{\partial \mathrm{OPD}(x, t)}{\partial x}\right|_{x=x_0} = -\frac{1}{U_C}\frac{d\mathrm{OPD}(x_0, t)}{dt}. \tag{18}$$

Recall that pupil-plane tilt results in a shifted irradiance pattern when focused onto the sensor. Therefore, if the beam is small enough, we can assume the measured deflection angles contain all the necessary information to obtain a meaningful estimate of $\mathrm{OPD}(x, t)$, such that $\mathrm{OPD}(x_0, t) = -U_C \int_0^t \theta_x(x_0, \tau)\mathrm{d}\tau$. Recognizing that the aberrations convect with an approximately known speed, we can then replace the temporal dimension with a pseudo-spatial coordinate, $\mathrm{OPD}(x_0, t) \rightarrow \mathrm{OPD}(x_0, x = -U_C t)$.

Gordeyev *et al.* [68] added a second laser beam, parallel and offset at a known distance Δx downstream from the first beam. The second beam enables the measurement of the convective velocity by cross correlating the time signals to obtain a time delay Δt. We can then calculate the convective velocity as $U_C = \Delta x/\Delta t$.

In practice, researchers perform the deflection angle measurements using a position sensing device (PSD) (aka lateral

position/displacement detector [32,69]). Since the PSD is an analog photosensitive crystal with a response time of less than 1 μs, it allows for sampling deflection angles at high sampling rates (up to a megahertz). We can also use high-speed cameras with reduced spatial resolution instead of PSDs to record the positions of the focused irradiance patterns. One obvious drawback of the Malley probe is that it only measures "slices" in the streamwise direction. Furthermore, it relies on the Taylor frozen flow assumption [70]. Therefore, this approach might yield inaccuracies in either spatially evolving fields such as the ones associated with linearly growing shear layers or in fields where discontinuities such as shock waves are present.

3. *Digital Holographic Wavefront Sensor*

The DHWFS works by interfering a signal beam with a reference beam [71]. In practice, both beams manifest from a master-oscillator laser. The signal beam propagates through aberrations, whereas the reference beam does not. Researchers use the sensor of a camera to measure the interference pattern (i.e., hologram). A digital hologram then becomes available for digital signal processing. Depending on the recording geometry [71–74], researchers can then use straightforward demodulation steps to obtain an estimate of the complex-optical field (both amplitude and wrapped phase).

The accuracy of this estimate in terms of the signal-to-noise ratio has been the subject of several recent studies for both continuous-wave [75–77] and pulsed [78–80] operation. With the use of a strong-reference beam, the DHWFS also enables a shot-noise-limited detection regime [81]. Researchers, in practice, can set the strength of the reference beam so that it boosts the signal beam well above the noise floor of the camera sensor.

Given a fixed number of camera-sensor pixels, the DHWFS typically has improved spatial resolution over the SHWFS [82]. Initial wind-tunnel experiments [83,84] have demonstrated the improved spatial resolution of the DHWFS over the SHWFS. However, more work needs to be conducted, especially in the presence of shock waves, which typically lead to phase discontinuities [61]. Such effects necessitate increased spatial resolution or the development of shock-wave-tolerant reconstructors [85].

Background oriented schlieren or "BOS" measurements show promise for increased spatio-temporal resolution at supersonic and hypersonic speeds [86–88]. Nonetheless, DHWFS measurements and computational-imaging techniques show distinct promise in sensing and correcting for the phase errors caused by aero-optical effects [89–94]. There has also been interest in using predictive filtering to increase imaging performance [95–99]. This last point leads us to the next section.

B. Imaging

There have been dedicated experimental test campaigns to study the image degradations caused by aero-optical effects. For example, Whiteley *et al.* and Gordeyev *et al.* [100,101] studied the effects of using a turret for imaging through various aerodynamic environments. Kalensky *et al.* [102] studied the effects of imaging through boundary layers and shear layers. Ding *et al.* [87] studied how aero-optical effects degrade one's ability to perform image-based targeting at hypersonic speeds. Many of these results used the modulation transfer function (MTF) measured from image data and estimated from SHWFS measurements. The MTF is an indication of an airborne-laser system's ability to discern contrast [103,104].

Recall that one can obtain the MTF from the point-spread function (PSF). In practice, the real-valued PSF is the irradiance (power per unit area) associated with the 2D Fourier transform of the collimated light that exists within a pupil plane of the laser system. Taking an additional 2D Fourier transform of the PSF provides the optical transfer function (OTF). One then obtains the real-valued MTF from taking the magnitude of the complex-valued OTF.

We present MTF results from Ref. [102] in Fig. 6 for imaging through boundary layers in $M = 0.5$ and 0.7 flow conditions, as well as imaging through shear layers for $M = 0.6$ and 0.7 flow conditions. Here, the x-axis is the normalized spatial frequency given as $\kappa\lambda Z/D$. We plot these results for the MTF calculated in the streamwise direction. We also plot the diffraction-limited MTF curve as a black dashed line for comparison. It should be noted that we estimated these MTF results from SHWFS measurements.

For the shear layer cases, Ref. [102] showed that image blurring was significant and occurred predominantly in the streamwise direction, as shown in Fig. 6. This blurring was due to organized vortical structures being present in the shear layers, which led to large-amplitude aberrations. Conversely, since the boundary layers are more benign in terms of aberration strength, there was not significant blurring in the data collected through the boundary layers. Additionally, as we show in part II of this two-part tutorial, the strength of the aberrations increases with the increasing Mach number. Consequently, imaging performance also degrades with the increasing Mach number.

Lastly, it is worth mentioning a distinction between imaging through aero-optical effects compared to atmospheric-optical effects. For the case of aerodynamic turbulence, all of the aberrations result from aero-optical effects that are in direct proximity to the aircraft. As such, these aberrations represent a thin optical-turbulence layer (relative to the length of the propagation path), and for that reason, we can approximate the phase errors as

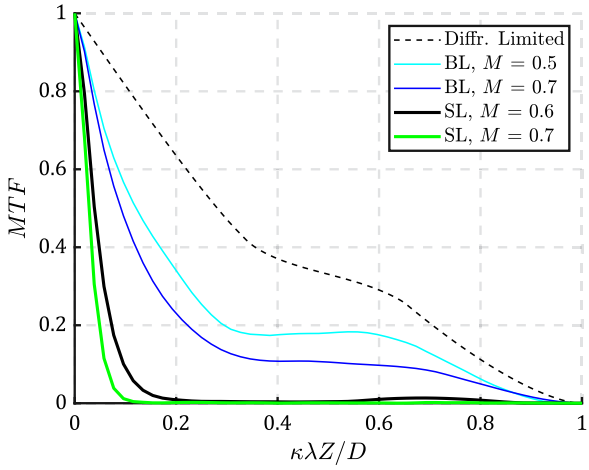

Fig. 6. MTF curves plotted for imaging through various boundary layers and shear layers. Adapted from Ref. [102] with permission.

Fig. 7. Various images of the AAOL test platform collected by M. Kalensky.

being isoplanatic. This outcome is in stark contrast to the path-integrated aberrations caused by atmospheric-optical effects, which can give rise to anisoplanatic phase errors [105–107]. For long propagation paths, the effects of scintillation can also play a role at the system level [108–110]. Together, the effects of scintillation and anisoplanatism tend to be the "Achilles' heel" to beam-control compensation [111].

5. CONCLUSION

In part I of this two-part tutorial, we started by introducing the concept of aero-optical effects in terms of aerodynamic turbulence, the Gladstone–Dale relation, quantifying their effects, and system performance. We then used a hemisphere-on-cylinder beam director as an example turret geometry. We showed that this turret gives rise to an aerodynamic environment that serves as a source for aberrations, and we decomposed these aberrations into piston, tilt, and higher-order phase errors. We also showed that the phase errors induced by aero-optical effects have adverse effects on system performance; however, we ultimately showed that we can ameliorate the associated performance degradations using phase compensation techniques. As a result, it is of utmost importance that system designers account for tilt and higher-order phase errors when designing future airborne-laser systems. This last point necessitates the use of wavefront sensing and imaging as part of the airborne-laser system's overall functionality. Thus, we introduced wavefront-sensing approaches that have both pioneered and continue to advance the field of aero-optics. We also discussed the performance impacts that aero-optical effects have on imaging performance. In part II of this two-part tutorial, we will build on the system-level considerations presented in part I. Specifically, we will survey several sources of aberrations such as boundary layers and shear layers, as well as mechanical contamination, shock waves, and aero-acoustics.

Acknowledgment. Advancements in the field of aero-optics are in part due to the Airborne Aero-Optics Laboratory (AAOL). In practice, the AAOL was an in-flight experimental test platform where aero-optics experiments could be performed under real conditions from which wind-tunnel testing and CFD results could be compared. These efforts afforded results that have supported research being conducted all over the world. A recent invited conference paper by the AAOL Program Director, E. Jumper, summarizes the total effort [112]. We present images taken by M. Kalensky of the AAOL test platform in Fig. 7.

Disclosures. The authors declare no conflicts of interest. The views expressed are those of the authors and do not necessarily reflect the official policy or position of the Department of the Air Force, Department of the Navy, the Department of Defense, or the U.S. Government. Approved for public release; distribution is unlimited. Public Affairs release approval # NSWCDD-PN-24-00132.

Data availability. Data underlying the results presented in this tutorial are not publicly available at this time.

REFERENCES

1. R. Duffner, *Airborne Laser: Bullets of Light* (Plenum Trade, 1997).
2. D. T. Kyrazis, "Airborne laser laboratory departure from Kirtland Air Force Base and a brief history of aero-optics," Opt. Eng. **52**, 071403 (2012).
3. H. Legner, J. Otis, G. Theophanis, *et al.*, "Laser beam degradation through turbulent interfaces," in *16th Aerospace Sciences Meeting* (AIAA, 1978), AIAA paper 1978-71.
4. D. Kelsall, "Optical measurements of degradation in aircraft boundary layers," in *Tech. rep.* (MIT, 1980).
5. G. Sutton, "On optical imaging through aircraft turbulent boundary layers," in *13th Fluid and PlasmaDynamics Conference* (AIAA, 1980).
6. B. Vu, G. Sutton, G. Theophanis, *et al.*, "Laser beam degradation through optically turbulent mixing layers," in *13th Fluid and PlasmaDynamics Conference* (AIAA, 1980), AIAA paper 1980-1414.
7. K. Gilbert, *Aero-Optical Phenomena* (American Institute of Aeronautics and Astronautics, 1982).
8. D. Bogdanoff, "The optical quality of shear layers: prediction and improvement thereof," AIAA J. **22**, 58–64 (1984).
9. G. W. Sutton, "Aero-optical foundations and applications," AIAA J. **23**, 1525–1537 (1985).
10. P. Cassady, S. Birch, and P. Terry, "Aero-optical analysis of compressible flow over an open cavity," AIAA J. **27**, 758–762 (1989).
11. E. J. Jumper and E. J. Fitzgerald, "Recent advances in aero-optics," Prog. Aerosp. Sci. **37**, 299–339 (2001).
12. E. J. Jumper and S. Gordeyev, "Physics and measurement of aero-optical effects: past and present," Annu. Rev. Fluid Mech. **49**, 419–441 (2017).
13. P. H. Merritt and J. R. Albertine, "Beam control for high-energy laser devices," Opt. Eng. **52**, 021005 (2012).
14. P. Merritt and M. Spencer, *Beam Control for Laser Systems*, 2nd ed. (Directed Energy Professional Society, 2018).
15. R. Duffner, *The Adaptive Optics Revolution* (University of New Mexico, 2009).
16. C. R. Truman and M. J. Lee, "Effects of organized turbulence structures on the phase distortion in a coherent optical beam propagating through a turbulent shear flow," Phys. Fluids **2**, 851–857 (1990).
17. C. Smith, C. Truman, and B. Masson, "Prediction of optical phase degradation using a turbulent transport equation for the variance of index-of-refraction fluctuations," in *28th Aerospace Sciences Meeting* (AIAA, 1990), AIAA paper 1990-250.
18. C. Truman, "The influence of turbulent structure on optical phase distortion through turbulent shear flows," in *Annual Interceptor Technology Conference* (AIAA, 1992), AIAA paper 1992-2817.
19. M. Malley, G. Sutton, and N. Kincheloe, "Beam-jitter measurements of turbulent aero-optical path differences," Appl. Opt. **31**, 4440–4443 (1992).
20. R. Hugo, E. J. Jumper, G. Havener, *et al.*, "Time-resolved wave front measurements through a compressible free shear layer," AIAA J. **35**, 671–677 (1997).
21. E. Fitzgerald and E. J. Jumper, "Aperture effects on the aerooptical distortions produced by a compressible shear layer," J. Aircraft **40**, 267–275 (2002).

22. M. Jones and E. Bender, "CFD-based computer simulation of optical turbulence through aircraft flowfields and wakes," in *32nd AIAA Plasmadynamics and Lasers Conference* (AIAA, 2001), AIAA paper 2001-2798.
23. P. Dimotakis, H. J. Catrakis, and D. Fourguette, "Flow structure and optical beam propagation in high-Reynolds-number gas-phase shear layers and jets," J. Fluid Mech. **433**, 105–134 (2001).
24. E. J. Fitzgerald and E. J. Jumper, "The optical distortion mechanism in a nearly incompressible free shear layer," J. Fluid Mech. **512**, 153–189 (2004).
25. H. J. Catrakis and R. Aguirre, "New interfacial fluid thickness approach in aero-optics with applications to compressible turbulence," AIAA J. **42**, 1973 (2004).
26. S. Gordeyev and E. Jumper, "Fluid dynamics and aero-optics of turrets," Prog. Aerosp. Sci. **46**, 388–400 (2010).
27. M. Wang, A. Mani, and S. Gordeyev, "Physics and computation of aero-optics," Annu. Rev. Fluid Mech. **44**, 299–321 (2012).
28. H. L. Ding, S. H. Yi, Y. Xu, *et al.*, "Recent developments in the aero-optical effects of high-speed optical apertures: from transonic to high-supersonic flows," Prog. Aerosp. Sci. **127**, 100763 (2021).
29. H. L. Ding, Z. H. Xia, S. H. Yi, *et al.*, "Research progress in aero-optical effects of supersonic turbulent shear layers," Prog. Aerosp. Sci. **146**, 101006 (2024).
30. M. W. Hyde, "Simulating random optical fields: tutorial," J. Opt. Soc. Am. A **39**, 2383–2397 (2022).
31. S. Avramov-Zamurovic, J. M. Esposito, and C. Nelson, "Classifying beams carrying orbital angular momentum with machine learning: tutorial," J. Opt. Soc. Am. A **40**, 64–77 (2023).
32. S. Gordeyev, E. J. Jumper, and M. R. Whiteley, *Aero-Optical Effects: Physics, Analysis and Mitigation* (Wiley, 2023).
33. V. I. Tatarskii, *Wave Propagation in a Turbulent Medium* (Dover Publications, 2016).
34. L. C. Andrews and R. L. Phillips, *Laser Beam Propagation Through Random Media*, 2nd ed. (SPIE, 2005).
35. D. L. Fried, "Optical resolution through a randomly inhomogeneous medium for very long and very short exposures," J. Opt. Soc. Am. **56**, 1372–1379 (1966).
36. D. Fried, "Optical heterodyne detection of an atmospherically distorted signal wave front," Proc. IEEE **55**, 57–77 (1967).
37. R. Q. Fugate, J. D. Barchers, and B. L. Ellerbroek, "David L. Fried: bringing vision to atmospheric optics [invited]," Appl. Opt. **62**, G112–G127 (2023).
38. Y. Diskin, M. Whiteley, M. Grose, *et al.*, "Aircraft to ground profiling: turbulence measurements and optical system performance modeling," AIAA J. **59**, 4610–4625 (2021).
39. M. Kalensky, E. J. Jumper, M. R. Kemnetz, *et al.*, "In-flight measurement of atmospheric-imposed tilt: experimental results and analysis," Appl. Opt. **61**, 4874–4882 (2022).
40. M. Kalensky, M. F. Spencer, E. J. Jumper, *et al.*, "Estimation of atmospheric optical turbulence strength in realistic airborne environments," Appl. Opt. **61**, 6268–6279 (2022).
41. J. H. Gladstone and T. P. Dale, "Researches on the refraction, dispersion, and sensitiveness of liquids," Philos. Trans. R. Soc. London **153**, 317–343 (1863).
42. J. H. B. Anderson, "Experimental determination of the gladstone-dale constants for dissociating oxygen," Phys. Fluids **12**, I-57–I-60 (1969).
43. H. Barrell and J. E. Sears, Jr., "The refraction and dispersion of air and dispersion of air for the visible spectrum," Philos. Trans. R. Soc. London Ser. A **238**, 1–64 (1939).
44. T. S. Ross, "Limitations and applicability of the Maréchal approximation," Appl. Opt. **48**, 1812–1818 (2009).
45. C. Porter, S. Gordeyev, and E. Jumper, "Large-aperture approximation for not-so-large apertures," Opt. Eng. **52**, 071417 (2013).
46. J. Pond and G. Sutton, "Aero-optic performance of an aircraft forward-facing optical turret," J. Aircraft **43**, 600–607 (2006).
47. N. De Lucca, S. Gordeyev, and E. Jumper, "The study of aero-optical and mechanical jitter for flat window turrets," in *50th AIAA Aerospace Sciences* (AIAA, 2012), AIAA paper 2012-623.
48. P. E. Morgan and M. R. Visbal, "Hybrid Reynolds-averaged Navier-Stokes/large-Eddy simulation investigating control of flow over a turret," J. Aircraft **49**, 1700–1717 (2012).
49. M. J. Krizo, S. J. Cusumano, S. T. Fiorino, *et al.*, "Design, development, and in-flight testing of a pointer/tracker for in-flight experiments to measure aero-optical effects over a scaled turret," Opt. Eng. **52**, 071415 (2013).
50. N. De Lucca, S. Gordeyev, and E. Jumper, "In-flight aero-optics of turrets," Opt. Eng. **52**, 071405 (2013).
51. C. Porter, S. Gordeyev, M. Zenk, *et al.*, "Flight measurements of the aero-optical environment around a flat-windowed turret," AIAA J. **51**, 1394–1403 (2013).
52. R. Jelic, S. Sherer, and R. Greendyke, "Simulation of various turrets at subsonic and transonic flight conditions using OVERFLOW," J. Aircraft **50**, 398–409 (2013).
53. J. Morrida, S. Gordeyev, N. D. Lucca, *et al.*, "Shock-related effects on aero-optical environment for hemisphere-on-cylinder turrets at transonic speeds," Appl. Opt. **56**, 4814–4824 (2017).
54. S. Gordeyev, N. D. Lucca, E. J. Jumper, *et al.*, "Comparison of unsteady pressure fields on turrets with different surface features using pressure-sensitive paint," Exp. Fluids **55**, 1661 (2014).
55. N. G. De Lucca, S. Gordeyev, J. J. Morrida, *et al.*, "Investigation of flow dynamics over turrets with different spanwise aspect ratios using PSP," in *SciTech Forum* (AIAA Aerospace Sciences Meeting, 2018), AIAA paper 2018-2047.
56. M. Kalensky, B. Catron, S. V. Gordeyev, *et al.*, "Investigation of aero-mechanical jitter on a hemispherical turret," Proc. SPIE **11836**, 1183606 (2021).
57. A. L. Roeder and S. Gordeyev, "Wake response downstream of a spanwise-oscillating hemispherical turret," J. Fluids Struct. **109**, 103470 (2022).
58. T. J. Bukowski, S. Gordeyev, M. Kalensky, *et al.*, "Study of unsteady surface flowfields on and around turrets with different protrusions," AIAA J. **61**, 5320–5331 (2023).
59. A. K. M. F. Hussain, "Coherent structures and turbulence," J. Fluid Mech. **173**, 303–356 (1986).
60. H. Sakamoto and H. Haniu, "A study on vortex shedding from spheres in a uniform flow," J. Fluids Eng. **112**, 386–392 (1990).
61. M. Kalensky, M. R. Kemnetz, and M. F. Spencer, "Effects of shock waves on Shack Hartmann wavefront sensor data," AIAA J. **61**, 2356–2368 (2023).
62. S. Gordeyev and M. Kalensky, "Effects of engine acoustic waves on aerooptical environment in subsonic flight," AIAA J. **58**, 5306–5317 (2020).
63. V. N. Mahajan, *Aberration Theory Made Simple* (SPIE, 1991).
64. R. J. Noll, "Zernike polynomials and atmospheric turbulence," J. Opt. Soc. Am. **66**, 207–211 (1976).
65. R. J. Sasiela, *Electromagnetic Wave Propagation in Turbulence: Evaluation and Application of Mellin Transforms* (SPIE, 2007).
66. J. P. Siegenthaler, "Guidelines for adaptive-optic correction based on aperture filtration," Ph.D. thesis (University of Notre Dame, 2008).
67. K. Taira, S. L. Brunton, S. T. M. Dawson, *et al.*, "Modal analysis of fluid flows: an overview," AIAA J. **55**, 4013–4041 (2017).
68. S. Gordeyev, E. Jumper, T.-M. Ng, *et al.*, "Aero-optical characteristics of compressible, subsonic turbulent boundary layers," in *Aviation Forum* (American Institute of Aeronautics and Astronautics, 2003).
69. S. Gordeyev, A. E. Smith, J. A. Cress, *et al.*, "Experimental studies of aero-optical properties of subsonic turbulent boundary layers," J. Fluid Mech. **740**, 214–253 (2014).
70. G. I. Taylor, "The spectrum of turbulence," Proc. R. Soc. **164**, 476–490 (1938).
71. M. F. Spencer, "Spatial heterodyne," in *Encyclopedia of Modern Optics*, 2nd ed., B. D. Guenther and D. G. Steel, eds. (Elsevier, 2018), pp. 369–400.
72. M. F. Spencer, R. A. Raynor, M. T. Banet, *et al.*, "Deep-turbulence wavefront sensing using digital-holographic detection in the off-axis image plane recording geometry," Opt. Eng. **56**, 031213 (2016).
73. M. T. Banet, M. F. Spencer, and R. A. Raynor, "Digital-holographic detection in the off-axis pupil plane recording geometry for deep-turbulence wavefront sensing," Appl. Opt. **57**, 465–475 (2018).
74. D. E. Thornton, M. F. Spencer, and G. P. Perram, "Deep-turbulence wavefront sensing using digital holography in the on-axis

phase shifting recording geometry with comparisons to the self-referencing interferometer," Appl. Opt. **58**, A179–A189 (2019).
75. D. E. Thornton, M. F. Spencer, C. A. Rice, *et al.*, "Digital holography efficiency measurements with excess noise," Appl. Opt. **58**, G19–G30 (2019).
76. D. E. Thornton, D. Mao, M. F. Spencer, *et al.*, "Digital holography experiments with degraded temporal coherence," Opt. Eng. **59**, 102406 (2020).
77. D. E. Thornton, M. F. Spencer, C. A. Rice, *et al.*, "Impacts of laboratory vibrations and laser flicker noise on digital holography," IEEE J. Quantum Electron. **56**, 1400107 (2020).
78. S. A. Owens, M. F. Spencer, D. E. Thornton, *et al.*, "Pulsed laser source digital holography efficiency measurements," Appl. Opt. **61**, 4823–4832 (2022).
79. S. A. Owens, M. F. Spencer, and G. P. Perram, "Digital-holography efficiency measurements using a heterodyne-pulsed configuration," Opt. Eng. **61**, 123101 (2022).
80. S. A. Owens, M. F. Spencer, and G. P. Perram, "Spectral broadening effects on pulsed-source digital holography," IEEE J. Quantum Electron. **59**, 8200109 (2023).
81. D. E. Thornton, C. J. Radosevich, S. Horst, *et al.*, "Achieving the shot-noise limit using experimental multi-shot digital holography data," Opt. Express **29**, 9599–9617 (2021).
82. D. E. Thornton, M. T. Banet, and M. F. Spencer, "Subaperture sampling for digital-holography applications involving atmospheric turbulence," Appl. Opt. **60**, G30–G39 (2021).
83. E. D. Chu, T. J. Bukowski, and S. Gordeyev, "Studies of local shock effects on Shack-Hartmann and digital holography wavefront sensors," Proc. SPIE **12693**, 1269317 (2023).
84. M. R. Kemnetz, M. Kalensky, T. E. DeFoor, *et al.*, "Experimental investigation into the effects of shock waves on Shack-Hartmann wavefront sensor measurements," Proc. SPIE **12693**, 1269314 (2023).
85. T. DeFoor, M. Kalensky, M. R. Kemnetz, *et al.*, "Shock-wave tolerant phase reconstructor for the Shack–Hartmann wavefront sensor," Proc. SPIE **12693**, 126930R (2023).
86. H. Ding, S. Yi, and X. Zhao, "Experimental investigation of aero-optics induced by supersonic film based on near-field background-oriented Schlieren," Appl. Opt. **58**, 2948–2962 (2019).
87. H. Ding, S. Yi, X. Zhao, *et al.*, "Experimental investigation on aero-optical effects of a hypersonic optical dome under different exposure times," Appl. Opt. **59**, 3842–3850 (2020).
88. H. Ding, S. Yi, Y. Xu, *et al.*, "Spatial structure similarity analysis of aero-optical wavefront induced by supersonic film cooling," AIAA J. **59**, 3773–3780 (2021).
89. S. T. Thurman and J. R. Fienup, "Phase-error correction in digital holography," J. Opt. Soc. Am. A **25**, 983–994 (2008).
90. C. J. Pellizzari, M. F. Spencer, and C. A. Bouman, "Phase-error estimation and image reconstruction from digital-holography data using a Bayesian framework," J. Opt. Soc. Am. A **34**, 1659–1669 (2017).
91. C. J. Pellizzari, M. T. Banet, M. F. Spencer, *et al.*, "Demonstration of single-shot digital holography using a Bayesian framework," J. Opt. Soc. Am. A **35**, 103–107 (2018).
92. S. T. Thurman, "Phase-error correction in digital holography using single-shot data," J. Opt. Soc. Am. A **36**, D47–D61 (2019).
93. C. J. Pellizzari, M. F. Spencer, and C. A. Bouman, "Coherent plug-and-play: digital holographic imaging through atmospheric turbulence using model-based iterative reconstruction and convolutional neural networks," IEEE Trans. Comput. Imaging **6**, 1607–1621 (2020).
94. C. J. Pellizzari, T. J. Bate, K. P. Donnelly, *et al.*, "Coherent plug-and-play artifact removal: physics-based deep learning for imaging through aberrations," Opt. Laser Eng. **164**, 107496 (2023).
95. S. Sulaiman, S. Gibson, and M. Spencer, "Predictive dynamic digital holography and image sharpening," J. Opt. Soc. Am. A **35**, 923–935 (2018).
96. S. Sulaiman, S. Gibson, and M. Spencer, "Subspace wavefront estimation using image sharpening and predictive dynamic digital holography," J. Opt. Soc. Am. A **37**, 1034–1042 (2020).
97. S. T. Thurman, P. Gatt, and T. Alley, "Wavefront sensing for anisotropic turbulence using digital holography," Proc. SPIE **9982**, 998205 (2016).
98. B. D. Shaffer, A. J. McDaniel, C. C. Wilcox, *et al.*, "Dynamic mode decomposition based predictive model performance on supersonic and transonic aero-optical wavefront measurements," Appl. Opt. **60**, G170–G180 (2021).
99. B. D. Shaffer, J. R. Vorenberg, C. C. Wilcox, *et al.*, "Generalizable turbulent flow forecasting for adaptive optics control," Appl. Opt. **62**, G1–G11 (2023).
100. M. R. Whiteley and D. J. Goorskey, "Imaging performance with turret aero-optical wavefront disturbances," Opt. Eng. **52**, 071410 (2013).
101. S. V. Gordeyev, N. G. D. Lucca, E. J. Jumper, *et al.*, "Image blurring due to turbulent wakes for airborne systems: flight tests," Proc. SPIE **10408**, 104080M (2017).
102. M. Kalensky, J. Wells, and S. Gordeyev, "Image degradation due to different in-flight aero-optical environments," Opt. Eng. **59**, 104104 (2020).
103. M. Roggemann, *Imaging Through Turbulence* (CRC Press, 1996).
104. J. Goodman, *Introduction to Fourier Optics*, 4th ed. (W. H. Freeman & Co., 2017).
105. D. L. Fried, "Anisoplanatism in adaptive optics," J. Opt. Soc. Am. **72**, 52–61 (1982).
106. R. J. Sasiela, "Strehl ratios with various types of anisoplanatism," J. Opt. Soc. Am. A **9**, 1398–1405 (1992).
107. J. Stone, P. H. Hu, S. P. Mills, *et al.*, "Anisoplanatic effects in finite-aperture optical systems," J. Opt. Soc. Am. A **11**, 347–357 (1994).
108. D. L. Fried, "Branch point problem in adaptive optics," J. Opt. Soc. Am. **15**, 2759–2768 (1998).
109. J. D. Barchers, D. L. Fried, D. J. Link, *et al.*, "Performance of wavefront sensors in strong scintillation," Proc. SPIE **4839**, 217–227 (2003).
110. M. T. Banet and M. F. Spencer, "Compensated-beacon adaptive optics using least-squares phase reconstruction," Opt. Express **28**, 36902–36914 (2020).
111. M. Kalensky, D. Getts, M. T. Banet, *et al.*, "Limitations of beam-control compensation," Opt. Express (2024).
112. E. J. Jumper, "The story of the Airborne aero-optics laboratory," Proc. SPIE **12239**, 122390G (2022).